

**The following resources related to this article are available online at [www.sciencemag.org](http://www.sciencemag.org) (this information is current as of October 19, 2009):**

**Updated information and services**, including high-resolution figures, can be found in the online version of this article at:

<http://www.sciencemag.org/cgi/content/full/325/5946/1405>

**Supporting Online Material** can be found at:

<http://www.sciencemag.org/cgi/content/full/325/5946/1405/DC1>

A list of selected additional articles on the Science Web sites **related to this article** can be found at:

<http://www.sciencemag.org/cgi/content/full/325/5946/1405#related-content>

This article **cites 22 articles**, 10 of which can be accessed for free:

<http://www.sciencemag.org/cgi/content/full/325/5946/1405#otherarticles>

This article has been **cited by** 1 articles hosted by HighWire Press; see:

<http://www.sciencemag.org/cgi/content/full/325/5946/1405#otherarticles>

This article appears in the following **subject collections**:

Neuroscience

<http://www.sciencemag.org/cgi/collection/neuroscience>

Information about obtaining **reprints** of this article or about obtaining **permission to reproduce this article** in whole or in part can be found at:

<http://www.sciencemag.org/about/permissions.dtl>

treated *gpr126<sup>st49</sup>* mutants with forskolin to elevate cAMP. Treatment with forskolin restored *oct6*, *krox20*, and *Mbp* expression (Fig. 4, A to L) and ultrastructurally normal myelin (fig. S11) in *gpr126<sup>st49</sup>* mutants, which suggests that Gpr126 functions to drive myelination by elevating cAMP levels in Schwann cells. Because *Krox20* is activated downstream of cAMP elevation, we would not expect forskolin treatment to rescue *Krox20* mutants. As a control, we therefore generated zebrafish *krox20* mutants by TILLING (19). Like murine *Krox20* mutants, Schwann cells in *krox20<sup>fh227</sup>* mutants are arrested at the promyelinating stage (7) (fig. S9); as expected, forskolin treatment did not rescue *Mbp* expression in *krox20<sup>fh227</sup>* mutants (Fig. 4, M to P). These data support the hypothesis that Gpr126 functions in Schwann cells to elevate levels of cAMP, thereby activating *oct6* and *krox20* expression to initiate myelination.

Our results show that Gpr126 is essential for Schwann cells to initiate myelination. Like most adhesion GPCRs, Gpr126 is an orphan receptor that has not been shown to interact with G proteins. Previously, a biochemical study raised the possibility that Gpr126 functions as a diffusible signal (20). Our data, however, suggest that Gpr126 acts as a receptor in Schwann cells that signals through G proteins to transiently elevate

cAMP. In Schwann cells, cAMP has been shown to activate a cascade including cAMP-dependent protein kinase (PKA), nuclear factor  $\kappa$ B, and cAMP response element-binding protein (CREB) to induce the transcription of *oct6* (21) (fig. S12). Our data show that Gpr126 acts autonomously in Schwann cells, that forskolin treatment is sufficient to restore myelination in *gpr126<sup>st49</sup>* mutants, and that *gpr126* is expressed independently of Nrg1/ErbB signals; hence, we propose that Gpr126 elevates cAMP in Schwann cells after axonal contact to trigger myelination.

#### References and Notes

1. K. R. Jessen, R. Mirsky, *Nat. Rev. Neurosci.* **6**, 671 (2005).
2. E. S. Monuki, G. Weinmaster, R. Kuhn, G. Lemke, *Neuron* **3**, 783 (1989).
3. S. S. Scherer et al., *J. Neurosci.* **14**, 1930 (1994).
4. T. S. Zorick et al., *Development* **126**, 1397 (1999).
5. M. Jaegle et al., *Science* **273**, 507 (1996).
6. J. R. Bermingham Jr. et al., *Genes Dev.* **10**, 1751 (1996).
7. P. Topilko et al., *Nature* **371**, 796 (1994).
8. C. Taveggia et al., *Neuron* **47**, 681 (2005).
9. H. M. Pogoda et al., *Dev. Biol.* **298**, 118 (2006).
10. R. Fredriksson et al., *Biochem. Biophys. Res. Commun.* **301**, 725 (2003).
11. T. K. Bjarnadottir et al., *Genomics* **84**, 23 (2004).
12. C. Stehlik et al., *FEBS Lett.* **569**, 149 (2004).
13. A. N. Garratt et al., *J. Cell Biol.* **148**, 1035 (2000).

14. G. V. Michailov et al., *Science* **304**, 700 (2004); published online 25 March 2004 (10.1126/science.1095862).
15. D. A. Lyons et al., *Curr. Biol.* **15**, 513 (2005).
16. S. Chen et al., *J. Neurosci.* **26**, 3079 (2006).
17. D. L. Sherman, P. J. Brophy, *Nat. Rev. Neurosci.* **6**, 683 (2005).
18. K. R. Jessen, R. Mirsky, L. Morgan, *Ann. N.Y. Acad. Sci.* **633**, 78 (1991).
19. C. B. Moens, T. M. Donn, E. R. Wolf-Saxon, T. P. Ma, *Brief. Funct. Genomics Proteomics* **7**, 454 (2008).
20. T. Moriguchi et al., *Genes Cells* **9**, 549 (2004).
21. J. Svaren, D. Meijer, *Glia* **56**, 1541 (2008).
22. F. Levavasseur et al., *Mech. Dev.* **74**, 89 (1998).
23. We thank members of the Talbot laboratory for helpful discussions and suggestions, T. Reyes and C. Hill for fish facility support, J. Perrino and J. Buchanan for electron microscopy advice, and E. Wolf-Saxon and T. Donn for identifying the *krox20<sup>fh227</sup>* mutation with the support of NIH grant HG002995 (C.B.M.). This work was also supported by National Multiple Sclerosis Society postdoctoral award FG 1719-A-1 (K.R.M.), a Stanford NIH training grant (T.D.G.), Telethon Italy fellowship GFP03011 (S.M.), a Stanford Gabilan fellowship (J.R.P.), and NIH grant R01 NS050223 and Muscular Dystrophy Association grant 92233 (W.S.T.). The GenBank accession number for zebrafish *gpr126* is GQ202546.

#### Supporting Online Material

www.sciencemag.org/cgi/content/full/325/5946/1402/DC1  
Materials and Methods

Figs. S1 to S12

References

12 March 2009; accepted 14 July 2009

10.1126/science.1173474

## Energy-Efficient Action Potentials in Hippocampal Mossy Fibers

Henrik Alle,<sup>1</sup>† Arnd Roth,<sup>2</sup> Jörg R. P. Geiger<sup>1\*</sup>

Action potentials in nonmyelinated axons are considered to contribute substantially to activity-dependent brain metabolism. Here we show that fast  $\text{Na}^+$  current decay and delayed  $\text{K}^+$  current onset during action potentials in nonmyelinated mossy fibers of the rat hippocampus minimize the overlap of their respective ion fluxes. This results in total  $\text{Na}^+$  influx and associated energy demand per action potential of only 1.3 times the theoretical minimum, in contrast to the factor of 4 used in previous energy budget calculations for neural activity. Analysis of ionic conductance parameters revealed that the properties of  $\text{Na}^+$  and  $\text{K}^+$  channels are matched to make axonal action potentials energy-efficient, minimizing their contribution to activity-dependent metabolism.

Energy expenditure due to mammalian brain activity is tightly linked to the generation and conduction of action potentials (APs), mainly in axons, and by the ensuing synaptic transmission. Estimation of the respective contributions to energy expenditure in the mammalian brain is the subject of controversy both at the cellular level (1–3) and at the level of non-

invasive imaging methods based on local metabolic rate changes (4, 5). The clarification of these controversies is important, for example, for the interpretation of functional magnetic resonance imaging data (6, 7). However, direct experimental data to determine the energy budget of APs in gray-matter axons, which are predominantly nonmyelinated (8), have been absent.

$\text{Na}^+$  influx during AP propagation increases  $\text{Na}^+$ - $\text{K}^+$ -adenosine triphosphatase (ATPase) activity and is thus proportional to energy (ATP) consumption. Current estimates of AP costs in mammals assume that the AP requires a fourfold  $\text{Na}^+$  charge compared to the charge necessary to depolarize a pure capacitor, the theoretical minimum (1–3, 9, 10). The factor of 4 relies on Hodgkin's notion (11), derived from the analysis

of squid giant axons, showing that inward  $\text{Na}^+$  and outward  $\text{K}^+$  currents overlap extensively during simulated APs (12), wasting  $\text{Na}^+$  and accordingly energy. Early data on nonmyelinated axons of different species obtained with radio-labeled  $\text{K}^+$ , however, cast doubt on the general applicability of Hodgkin's notion (13).

To experimentally investigate the energetics of axonal APs in the mammalian cortex, it is essential to measure, at physiological temperatures, the ion fluxes underlying axonal APs, which differ from somatic APs (14, 15), as might the underlying currents (16, 17). Patch-clamp recordings at 36° to 37°C from rat hippocampal mossy fiber boutons (MFBs, Fig. 1A) (14, 18), which are presynaptic expansions of nonmyelinated mossy fibers (19), revealed brief APs ( $249 \pm 4 \mu\text{s}$  half-duration,  $n = 14$ ; Fig. 1A and fig. S1), resembling neocortical axonal APs (15). Ionic currents underlying the AP were determined by applying a previously recorded AP wave (Fig. 1B, black trace) as a voltage command (20) to outside-out patches from MFBs.  $\text{Na}^+$  currents ( $I_{\text{Na}}$ ) showed rapid activation and fast decay (decay time constants =  $24 \pm 3 \mu\text{s}$ ,  $0.80 \pm 0.03$  amplitude contribution; and  $130 \pm 12 \mu\text{s}$ ,  $0.20 \pm 0.03$  amplitude contribution; Fig. 1, B and C, red traces; fig. S1,  $n = 8$ ). The onset of  $\text{K}^+$  currents ( $I_{\text{K}}$ ; Fig. 1, B and C, blue traces;  $n = 8$ ) was significantly delayed compared to that of  $I_{\text{Na}}$  ( $106 \pm 5 \mu\text{s}$ ;  $P < 0.001$ ), similar to results obtained from whole-bouton recordings (Fig. 1D,  $115 \pm 7 \mu\text{s}$ ;  $P < 0.001$ ,  $n = 8$ ;  $P > 0.5$  for patch versus whole-bouton recording). The resulting

<sup>1</sup>Independent Hertie Research Group, Max-Planck-Institute for Brain Research, 60528 Frankfurt, Germany. <sup>2</sup>Wolfson Institute for Biomedical Research, University College London, Gower Street, London WC1E 6BT, UK.

\*Present address: Institute of Neurophysiology, Neuroscience Research Center, Charité-Universitätsmedizin Berlin, Charité-platz 1, 10117 Berlin, Germany.

†To whom correspondence should be addressed. E-mail: henrik.alle@charite.de

small overlap of inward and outward currents [Fig. 1, B (inset) and C] indicated a high  $\text{Na}^+$  efficiency and, accordingly, energy efficiency in

hippocampal mossy fibers, contrasting with previous simulations of axonal APs and their underlying currents (12, 17, 21).

To complement these results by a quantitative assessment of the  $\text{Na}^+$  influx as well as peak  $\text{Na}^+$  and  $\text{K}^+$  conductance densities ( $G_{\text{Na}}$  and  $G_{\text{K}}$ ) underlying an AP propagating along an axon, we performed numerical simulations of APs. We used conductance functions (Fig. 2A) derived from recorded currents (Fig. 1) in a compartmental model of the mossy fiber (18) to reconstitute propagating APs (22). Simulations resulted in AP waveforms and underlying currents closely resembling recorded APs and currents (Fig. 2B and fig. S1, A to D). The validity of our approach was further tested with independent predictions of the model, such as  $I_{\text{Na}}$  onset potential and AP propagation velocity, which both complied with experimental data (Fig. 2C and fig. S2). The charge separation, measured as the ratio of nonoverlapping to total  $\text{Na}^+$  charge per AP (Fig. 1B, inset), amounted to  $0.79 \pm 0.03$  in the simulations ( $n = 8$ ), consistent with a value of  $0.80 \pm 0.02$  obtained from patch data ( $n = 8$ ; Fig. 2, B and D) (22). The resulting mean value of  $G_{\text{Na}}$  peak amplitudes was  $39 \pm 3 \text{ mS/cm}^2$ , in good agreement with previous results (16), and that of  $G_{\text{K}}$  peak amplitudes was  $7.8 \pm 0.3 \text{ mS/cm}^2$  ( $n = 8$ , respectively). The mean  $\text{Na}^+$  charge transfer per propagating AP was  $153 \pm 6 \text{ nC/cm}^2$  ( $n = 8$ ), being only 1.3 times the theoretical minimum (Fig. 2E;  $n = 8$ ) of  $121 \text{ nC/cm}^2$  for a target AP amplitude of  $121 \text{ mV}$  [specific membrane capacitance ( $C_m$ )  $1 \mu\text{F/cm}^2$ ], which is considerably less than the factor of 4 used in the literature (1–3, 9, 10). The corresponding  $1.6 \pm 0.1 \text{ pmol}$  of  $\text{Na}^+$  ions/ $\text{cm}^2$  per AP is close to earlier estimates for nonmyelinated axons of diverse species but not to data from the squid giant axon (13), causing an

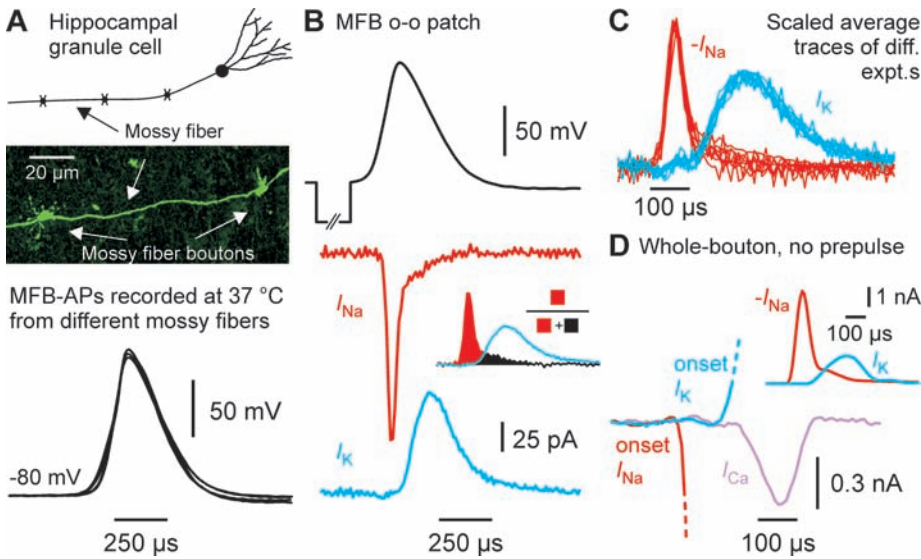
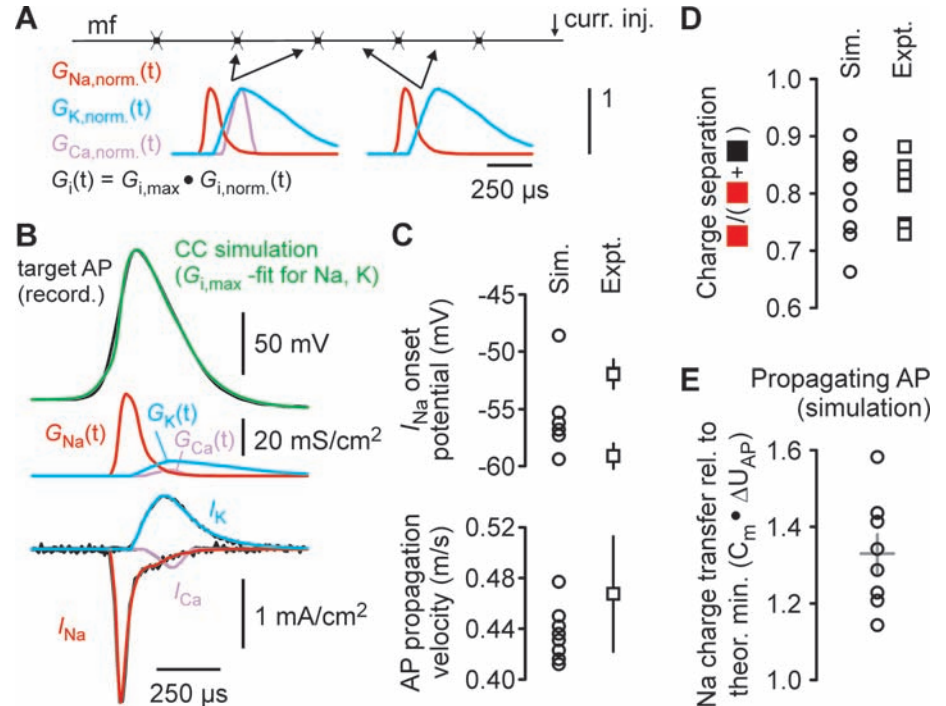


**Fig. 1.** Temporal separation of transmembrane currents during the MFB AP at  $36^\circ$  to  $37^\circ\text{C}$ . **(A)** (Top) Sketch of a hippocampal granule cell (mossy fiber truncated). (Middle) Fluorescence image of a hippocampal mossy fiber with presynaptic expansions (MFBs and filopodial extensions). (Bottom) MFB-APs from different experiments. **(B)** Upper trace, MFB-AP as voltage command to outside-out patches of MFBs. Middle trace, isolated  $I_{\text{Na}}$  (in  $1 \text{ mM}$  4-AP). Bottom trace, isolated  $I_{\text{K}}$  (in  $1 \mu\text{M}$  TTX). Recordings were made from different patches. The inset defines the measure of charge separation:  $\text{Na}^+$  charge that is not counterbalanced by simultaneously flowing  $\text{K}^+$  charge divided by total  $\text{Na}^+$  charge per AP. **(C)** Average  $I_{\text{Na}}$  of different experiments inverted and overlaid on average  $I_{\text{K}}$  of different experiments (scaled to the mean amplitude of all  $I_{\text{Na}}$  or  $I_{\text{K}}$ , respectively), indicating the experimental range of current kinetics across patches. **(D)** Relative timing of  $I_{\text{Na}}$  onset,  $I_{\text{K}}$  onset, and the presynaptic  $I_{\text{Ca}}$  (in TTX and 4-AP) in response to the MFB-AP wave (without prepulse) recorded in the whole-bouton configuration. Recordings were made from different MFBs. (Inset) Whole-bouton  $I_{\text{Na}}$  and  $I_{\text{K}}$ , scaled to the respective mean of the amplitudes of all whole-bouton  $I_{\text{Na}}$  or  $I_{\text{K}}$  experiments.

**Fig. 2.** Reconstitution modeling of recorded APs reveals close to minimum  $\text{Na}^+$  charge transfer during propagating APs. **(A)** (Top) Schematic mossy fiber (mf). Curr. inj., current injection site in current-clamp simulation. (Bottom) Experimentally derived, normalized Na, K, and Ca conductance time courses from current measurements in Fig. 1B ( $I_{\text{Na}}$  and  $I_{\text{K}}$ ) and Fig. 1D ( $I_{\text{Ca}}$ ). **(B)** (Top) MFB-AP from current clamp simulation (green) superimposed on the recorded target MFB-AP of Fig. 1B (black). (Middle) Peak conductance densities obtained from fit. (Bottom) Currents underlying the simulated AP, superimposed on the recorded currents (black) of Fig. 1B ( $I_{\text{Na}}$  and  $I_{\text{K}}$ ) and Fig. 1D ( $I_{\text{Ca}}$ ). **(C)** (Top) Comparison of the range of  $\text{Na}^+$  current onset potentials in simulations and patch experiments. (Bottom) AP conduction velocities in simulations compared to experimentally determined velocities (at  $36^\circ$  to  $37^\circ\text{C}$ ). **(D)** Charge separation as defined in Fig. 1B, inset, in simulations and patch experiments. **(E)** Costs of a propagating AP in simulations expressed as  $\text{Na}^+$  charge transfer per AP relative to the theoretical minimum of charging a pure capacitor to a voltage difference equaling the AP amplitude. Circles indicate individual simulations; the cross indicates the mean  $\pm$  SEM (error bars indicate SEM).



absolute energy demand per AP of  $\sim 0.53 \pm 0.02$  pmol of ATP/cm<sup>2</sup> [assuming that the Na<sup>+</sup>-K<sup>+</sup>-ATPase transports three Na<sup>+</sup> ions per ATP molecule; for comparison to the costs of preserving a resting membrane potential of  $-80$  mV and an estimate of the required Na<sup>+</sup>-K<sup>+</sup>-ATPase density, see (22)]. Thus, the energy expenditure associated with mossy fiber APs themselves is only about one-third of that hitherto assigned to nonmyelinated axons of the mammalian brain (1, 3, 10).

How critical are conductance parameters such as  $G_{Na}$  decay time and  $G_K$  onset delay in determining the energy efficiency of mossy fiber APs? The AP reconstitution approach constrained by recorded target APs enabled us to systematically analyze the dependence of Na<sup>+</sup> influx per AP on different combinations of the two modified conductance parameters. In the majority of combinations (20 out of 25), the amplitude, half-duration, and propagation velocity of simulated APs were consistent with those of recorded APs [Fig. 3, A and D (yellow and

purple circles)]. These APs represented functionally equivalent signals with respect to information transmission but differed considerably with respect to underlying currents and the Na<sup>+</sup> charge relative to the theoretical minimum (Fig. 3E, yellow and purple bars), ranging from 1.1 to 3.2. The results were reproduced in a cylindrical axon, indicating independence of morphology, axon diameter, and basic electrophysiological properties (figs. S3 and S4). We also obtained APs that slightly failed to reach either the amplitude or the half-duration of recorded APs (Fig. 3, B to E, gray circles and bars). Among these, the energetically most expensive combination (Fig. 3B) was reminiscent of Hodgkin and Huxley's simulated currents underlying the AP and associated deviations of the simulated from the recorded APs of the squid giant axon (12). Conductance combinations that matched experimentally derived  $G_{Na}$  decay times and  $G_K$  onset delays and that resulted in AP shapes consistent with recordings were among those

which displayed a minimized Na<sup>+</sup> charge cost (Fig. 3E, yellow bars).

In addition, the fit results for the different conductance parameter combinations in Fig. 3E also varied with respect to  $G_{Na}$  and  $G_K$  peak amplitudes. Conductance parameter combinations containing a fast  $G_{Na}$  decay and long  $G_K$  onset delay as observed experimentally result in comparatively low  $G_{Na}$  and  $G_K$  peak amplitudes (Fig. 3F, yellow circles). Thus, the observed degrees of charge separation are accompanied by comparatively low peak conductance densities, suggesting low numbers of channel proteins per area, which would minimize infrastructural costs for AP conduction. Taken together, both the fast decay of  $G_{Na}$  and the precisely matched delay of  $G_K$  onset at the mossy fiber optimize the energy efficiency of axonal APs. AP amplitude, shape, and propagation velocity were rather insensitive to a variety of combinations of conductance parameters, which implies that physiological descriptions of APs require the reconstitution not only of APs but also of underlying currents.

To relate the costs of APs themselves as determined above to downstream costs in the hip-

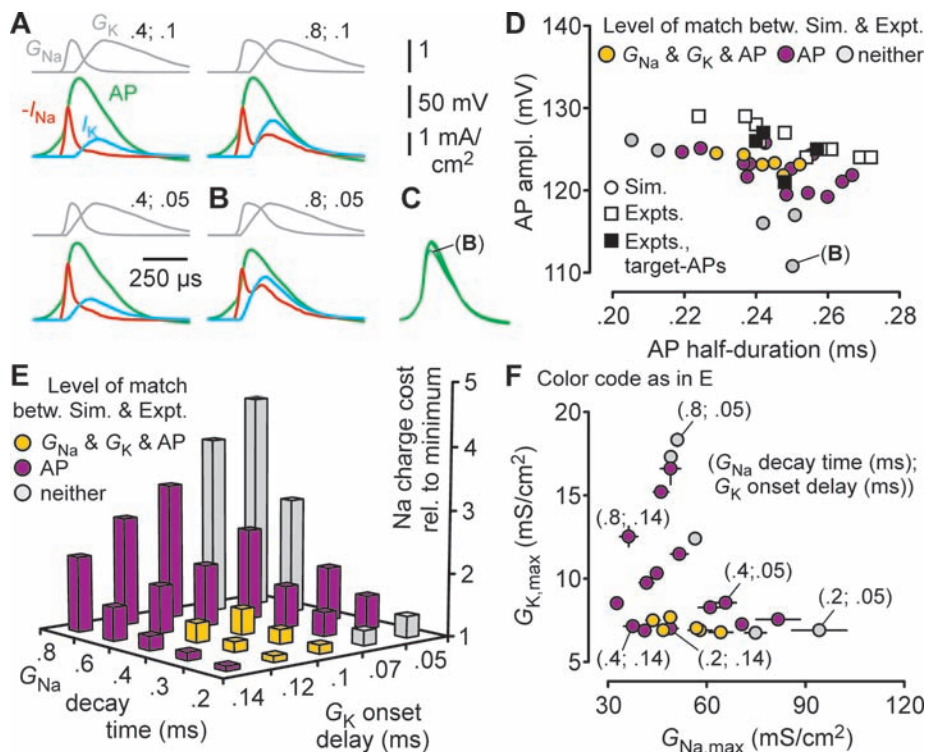


**Fig. 3.** Experimentally revealed conductance properties optimize AP-related Na<sup>+</sup> charge transfer and thus energy demand in simulations. (A) Gray traces indicate modifications of the normalized  $G_{Na}$  and  $G_K$  time courses of Fig. 2A; first number,  $G_{Na}$  decay time (peak to zero amplitude; in milliseconds); second number,  $G_K$  onset delay (in milliseconds) from  $G_{Na}$  onset. Colored traces, resulting  $I_{Na}$  (red) and  $I_K$  (blue), superimposed on the resulting simulated AP (green). (B) Example of a simulation in which the parameter combination resulted in a poor reconstitution of the recorded target AP. (C) Overlay of the simulated APs of (A) and (B) [on a different time scale than in (A) and (B)]. (D) Distribution of AP amplitude and half-duration of recorded APs (Expt., squares) and of simulated APs (Sim., circles). Black squares indicate target APs used for the fits in Fig. 3, D to F. (E) AP cost expressed as Na<sup>+</sup> charge transfer per AP relative to the theoretical minimum for different combinations of ionic conductance parameters. The color code indicates the level of match between simulations and experiments with respect to conductance parameters (chosen for the simulation) and AP (amplitude and half-duration; simulation result). (F) Best-fit, AP wave-evoked peak  $G_{Na}$  and  $G_K$  densities of the simulations in (D) and (E). Numbers in parentheses indicate the ionic conductance parameter combination. Error bars indicate SEM.

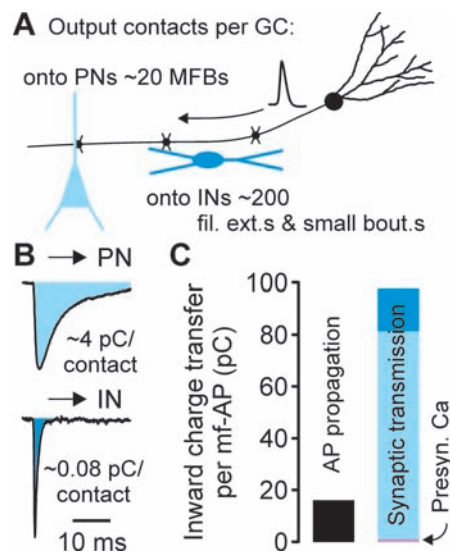


**Fig. 4.** The charge transfer related to synaptic transmission in the hippocampal mossy fiber system is considerably larger than that for APs. (A) Schematic diagram of the hippocampal mossy fiber system. GC, granule cell; PN, principal neuron (light blue); IN, interneuron (dark blue); fil. ext., filopodial extensions; bout., boutons. (B) Examples of unitary AMPA receptor-mediated currents (black) at two types of output synapses and the average charge transfer per contact (blue shaded areas; GC-CA3 pyramidal neuron synapse and GC-dentate gyrus basket cell synapse). (C) Summary of the respective total charge transfers related to propagation of a single mossy fiber AP (left bar), ensuing presynaptic Ca<sup>2+</sup> entry (right bar, purple) and postsynaptic cation inflow (right bar, blue) in response to the mossy fiber AP, mediated by ligand-gated glutamate receptors in PNs (light blue) and INs (dark blue).

pocampal mossy fiber system, we analyzed the presynaptic  $\text{Ca}^{2+}$  influx (Figs. 1D and 2B) and the inward charge transfer mediated by unitary AMPA receptor-mediated excitatory currents in different postsynaptic neuron types (Fig. 4, A and B) (18, 23). From these data, we calculated that the cost ratio of the mossy fiber AP itself to the downstream events (Fig. 4) has an upper limit of about 0.15 (22), shifting the emphasis of activity-dependent energy demand to downstream processes elicited by transmitter release, as suggested by in vivo work (4, 6, 7).

Assuming a widespread occurrence of a high degree of charge separation during APs in axons, our results could resolve disparities between systemic in vivo studies (4, 6, 7) and bottom-up energy budget calculations (1–3). Our findings challenge the general applicability of Hodgkin's notion (1–3, 9, 10) to gray-matter nonmyelinated axons but are in line with considerations that in evolution, the economy of neural processes tends to be optimized (24).

#### References and Notes

1. D. Attwell, S. B. Laughlin, *J. Cereb. Blood Flow Metab.* **21**, 1133 (2001).
2. D. Attwell, C. Iadecola, *Trends Neurosci.* **25**, 621 (2002).
3. P. Lennie, *Curr. Biol.* **13**, 493 (2003).
4. J. Niessing *et al.*, *Science* **309**, 948 (2005).
5. R. Mukamel *et al.*, *Science* **309**, 951 (2005).
6. N. K. Logothetis, *Nature* **453**, 869 (2008).
7. S. Mangia *et al.*, *J. Cereb. Blood Flow Metab.* **29**, 441 (2009).
8. V. Braitenberg, A. Schüz, *Cortex: Statistics and Geometry of Neuronal Connectivity* (Springer, Berlin, ed. 2, 1998).
9. J. C. Nawroth, C. A. Greer, W. R. Chen, S. B. Laughlin, G. M. Shepherd, *J. Neurosci.* **27**, 9790 (2007).
10. S. S.-H. Wang *et al.*, *J. Neurosci.* **28**, 4047 (2008).
11. A. L. Hodgkin, *Philos. Trans. R. Soc. London Ser. B* **270**, 297 (1975).
12. A. L. Hodgkin, A. F. Huxley, *J. Physiol.* **117**, 500 (1952).
13. J. M. Ritchie, *Prog. Biophys. Mol. Biol.* **26**, 147 (1973).
14. J. R. P. Geiger, P. Jonas, *Neuron* **28**, 927 (2000).
15. M. H. P. Kole, J. J. Letzkus, G. J. Stuart, *Neuron* **55**, 633 (2007).
16. D. Engel, P. Jonas, *Neuron* **45**, 405 (2005).
17. Y. Yu, Y. Shu, D. A. McCormick, *J. Neurosci.* **28**, 7260 (2008).
18. H. Alle, J. R. P. Geiger, *Science* **311**, 1290 (2006).
19. L. Acsady, A. Kamondi, A. Sik, T. Freund, G. Buzsáki, *J. Neurosci.* **18**, 3386 (1998).
20. B. P. Bean, *Nat. Rev. Neurosci.* **8**, 451 (2007).
21. A. A. Faisal, S. B. Laughlin, *PLoS Comput. Biol.* **3**, e79 (2007).
22. Materials and methods are available as supporting material on Science Online.
23. J. R. P. Geiger, J. Lübke, A. Roth, M. Frotscher, P. Jonas, *Neuron* **18**, 1009 (1997).
24. S. B. Laughlin, T. J. Sejnowski, *Science* **301**, 1870 (2003).
25. We thank A. Lampert and C. Schmidt-Hieber for discussion on sodium conductances and M. Häusser for comments on the manuscript. This work was supported by the Max Planck Society, the Hertie Foundation, the Deutsche Forschungsgemeinschaft (AL 1193/2-1), and the Engineering and Physical Sciences Research Council.

#### Supporting Online Material

[www.sciencemag.org/cgi/content/full/325/5946/1405/DC1](http://www.sciencemag.org/cgi/content/full/325/5946/1405/DC1)

Materials and Methods

Figs. S1 to S4

References

31 March 2009; accepted 31 July 2009

10.1126/science.1174331